The Functional Logic of Odor Information Processing in the *Drosophila* Antennal Lobe

Aurel A. Lazar, Tingkai Liu, Chung-Heng Yeh
Bionet Group
Department of Electrical Engineering
Columbia University

December 27, 2021

Abstract

In the early olfactory pathway of *Drosophila*, Olfactory Sensory Neurons (OSNs) multiplicatively encode the odorant identity and the concentration profile. Projection Neurons (PNs) responses in the Antennal Lobe (AL), in turn, exhibit strong transients at odorant onset/offset and stable steady-state behavior. What is the functional logic the of diverse set of Local Neurons (LNs) in the AL? Addressing this question may shed light on the key characteristics of odor information processing in the AL, and odorant recognition and olfactory associative learning in the downstream neuropils of the early olfactory system.

To address the computation performed by each LN type, we exhaustively evaluated all circuit configurations of the Antennal Lobe. We found that, across model parameterizations, presynaptic inhibition of the OSN-to-PN synapse is essential for odorant identity recovery in steady-state, while postsynaptic excitation and inhibition facilitate on-/off-set event detection. The onset and offset events indicate changing odorant identities, and together with the identity recovery in steady-state, suggest that the AL is an *event-based odorant identity recovery processor*.

Contents

1 Introduction **3**

2 Results **5**
2.1 Processing Monomolecular Odorants in the Antennal Lobe 5
2.2 Presynaptic and Postsynaptic Local Neurons Enable Concentration Invariance and Contrast Boosting in Temporal Processing of Single Channels 7
2.3 Spatio-Temporal Processing of Odorant Waveforms 11

3 Discussion **18**

4 Materials and Methods **20**
4.1 Decomposing OSN and PN responses into steady-state and transient components 20
4.2 Metrics 21
4.3 Biophysical Models and Parameterizations 22
4.4 Optimization Objectives 23
4.5 Two-Step Optimization Procedure 25

5 Appendix **30**
5.1 Temporal Processing of Mono-molecular Odorants Figure Supplements 30
5.2 Spatio-Temporal Processing of Mono-molecular Odorants Figure Supplements 33

1 Introduction

The early olfactory system of the fruit fly interacts with the complex odorant landscape[1], encoding both the odorant identity and the odorant concentration waveform [2] into a combinatorial neural code at the level of Olfactory Sensory Neurons (OSNs) in the Antenna. The odor information processing in the Antennal Lobe (AL) and its resulting representation by the Projection Neurons (PNs), in turn, is further processed in higher brain centers for feature recognition, associative learning, and other cognitive tasks [3, 4, 5]. Due to the multiplicative coupling between the odorant identity and the concentration profile [6, 2] (see **Fig.**1(A)), the OSN response to odorant waveforms is a confounding representation between identity and concentration [7, 8]. Robust odorant recognition and olfactory associative learning, therefore, requires the AL circuit to generate concentration-invariant PN spatio-temporal responses across odorant identities (**Fig.**1(A)) [9, 10, 11]. Indeed, as shown in **Fig.**1(B), PN responses exhibit strong transients [12] and stable steady-state behavior. The natural question that arises here is how is such behavior carried out by the AL circuit.

Structurally, the Antennal Lobe (AL) is tiled, in 3-dimensions, by 50 sub-neuropil structures (glomeruli) comprised of the axons of OSNs and the dendrites of PNs [13, 14, 15]. As the OSNs innervating each glomerulus express the same odorant receptor type [15, 6], the channels in the early olfactory pathway, formed by OSNs & PNs innervating the same glomerulus, implement a parallel processing model of odor signal processing organized by receptor types [3]. Importantly, computations both within and between channels in the Antennal Lobe is facilitated by about 120 local neurons (LNs) [16, 17, 18, 19, 20, 21] that are differentiated by their innervating patterns (within vs. across glomeruli) and excitatory/inhibitory synapses. While the synapse-level connectome of the AL has provided invaluable insight into the diversity of LNs in both the adult [22] and larva [23] AL, the specific computational role of each of the LN types remains unknown.

To explore the neural basis of odor signal processing in the AL, we considered 3 main LN cell types: 1) pre-synaptic (to an OSN-to-PN synapse) pan-glomerular (innervating all glomeruli) inhibitory LNs (Pre-LNs), 2) post-synaptic (to an OSN-to-PN synapse) uni-glomerular (innervating a single glomerulus) excitatory LNs (Post-eLNs), and 3) post-synaptic uni-glomerular inhibitory LNs (Post-iLNs). Via massively parallel simulations (Methods), we exhaustively evaluated single-channel and multi-channel AL circuit models with all variations of LN connectivity (local vs. global, feedforward vs. feedback). To provide a rigorous evaluation of computations inherent to the model structure, random samples of the parameter space for

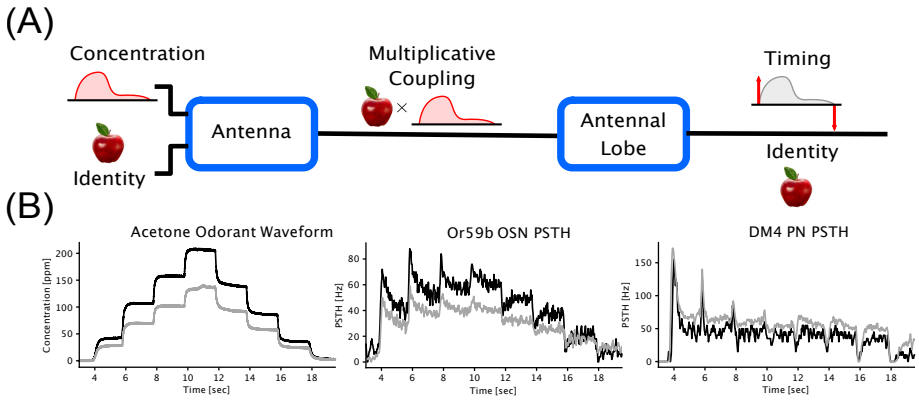

Figure 1: Olfactory processing in and circuit schematic of the Antennal Lobe. (A) Computational logic of the olfactory pathway. The Antenna encoding of odorant waveforms is confounded between odorant identity and concentration. For robust downstream odor signal processing, recognition and associative learning, the Antennal Lobe transforms the confounded Antenna odorant representation into on/offset timing information and recovers the odorant identity. (B) Input/Output (I/O) characteristics of the early olfactory pathway. Shown from left to right are the Acetone staircase odorant waveforms, Or59b OSN PSTHs and DM4 PN PSTHs, respectively. Data taken from [24].

each circuit were performed to compare the circuit performances across parametrizations.

We found that inhibition from the Pre-LN across glomeruli is essential in reducing concentration-dependencies of the responses of PNs allowing odorant identities to be stably recovered as odorant affinity vectors. On the other hand, excitation and inhibition from Post-eLNs and Post-iLNs capture onset and offset input transients, respectively (see **Fig.**1(B) for circuit schematic).

Together, the onset/offset events detection by the Post-LNs and the identity recovery by the Pre-LN support an *event-driven odorant identity recovery* processing paradigm for the AL, enabling rapid and robust odorant recogition and olfactory associative learning downstream.

2 Results

2.1 Processing Monomolecular Odorants in the Antennal Lobe

To investigate the functional logic of odor signal processing in the Antennal Lobe, we begin by reviewing how the odorant identity and concentration profile for a single odorant-receptor pair is represented in the OSNs. Following [2], the identity of a monomolecular odorant is characterized by the parameters:

1. *binding rate* $[\mathbf{b}]_{ron}$, i.e., the strength a given odorant molecule o binds to the receptors of type $r = \{1, 2, \ldots, R\}$ expressed by OSN n, and
2. *dissociation rate* $[\mathbf{d}]_{ron}$, i.e., the rate at which the odorant molecule o dissociates from its previously bound odorant receptors of type r expressed by OSN n.

Since the binding and dissociation rates for OSNs expressing the same receptor type (along index n) captures their intrinsic sensing capability, they fully characterize odorant <u>identity</u>. However, as olfactory stimuli are transmitted via odorant plumes with a time varying concentration profile, the activation of olfactory receptors as described in [2] is also dependent on the concentration waveform $u(t)$ leading to the odorant input model

$$([\mathbf{b}]_{ron} \cdot u(t), [\mathbf{d}]_{ron}),$$

that is encoded by the OTP-BSG cascade model of the OSN [2].

However, as shown in [2], the steady-state response of the OTP-BSG cascade model only depends on $[\mathbf{b}]_{ron}/[\mathbf{d}]_{ron} \cdot u(t)$, while the transient response depends on both the aforementioned variable and the dissociation rate. It is therefore often more convenient to characterize an odorant with the string

$$([\mathbf{b}]_{ron}/[\mathbf{d}]_{ron} \cdot u(t), [\mathbf{d}]_{ron}), \tag{1}$$

where $([\mathbf{b}]_{ron}/[\mathbf{d}]_{ron})$ is the *affinity rate* [2]. This characterization also suggests that the odorant identity (affinity and dissociation rates) can be extracted by respectively analyzing the steady-state and transient responses of the OSNs and PNs.

Leveraging the physiology recordings of Or59b OSN and DM4 PN responses to Acetone odorant staircase concentration waveforms (2 of the 7 stimulus-response pairs are shown in **Fig.**1(B)), we extracted the steady-state and transient responses for both OSNs and PNs (**Fig.**2(B), see Methods for details). We observe that the PN responses differ from the OSN responses in 2 important ways:

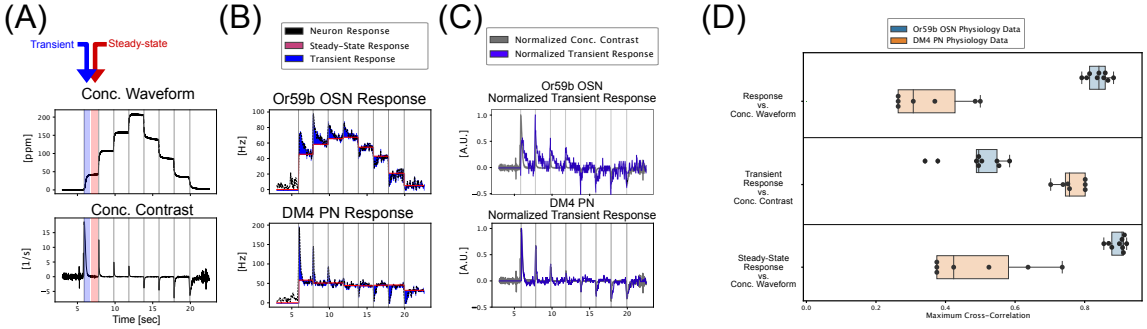

Figure 2: Essential temporal encoding/processing characteristics of the DM4 PNs. (A) Acetone concentration waveform (first published in [24]) and concentration contrast (see **Eq.**(2)), $\varepsilon = 1$. (B) Or59b OSN and DM4 PN spike train data in response to an Acetone staircase waveform. Each neuron response is decomposed into steady-state and transient responses - where the steady-state response is computed as the average PSTH within a 500 milisecond window before change in odorant concentration. The transient response is the residual obtained by subtracting the steady-state response from the overall response. See the text for more details. (C) Neuron normalized transient response compared against normalized concentration contrast in (C1 bottom). Note that the PN transient response agrees very well with concentration contrast. (D) Maximum cross-correlation between different representations of odorant concentration waveforms (i.e., gradient, contrast) and different representations of neuron/model responses (i.e., transient steady-state). Shown here is $\max_\tau \int x(t)y(t+\tau)dt$, where $x(t)$ is the steady-state/transient neuron response and $y(t)$ is the concentration waveform/contrast.

- *Concentration Invariance*: Compared with OSN responses during steady-state, PN responses show significantly lower dependency on concentration waveform. In addition to the visual comparison of OSN and PN steady-state responses in **Fig.**2(B), we computed the Maximum Cross-Correlation (see Methods) between the steady-state OSN/PN responses and the odorant concentration waveform for each stimulus-response pair. The results for Or59b OSNs and DM4 PNs, shown as box-plots in **Fig.**2(D, bottom row), show a significantly lower maximum correlation for PNs as compared to OSNs, indicating a reduction in concentration dependency of the PN.

- *Contrast Boosting*: The PN response during transients is stronger in amplitude and faster in dynamics than the OSN response. We observe, in **Fig.**2(C), that the PN transient response closely resembles the "contrast" of the odorant waveform. Depicted in **Fig.**2(A bottom), the concentration contrast of the staircase waveform is given as:

$$\text{Contrast}[u](t) = \frac{du/dt}{\epsilon + u(t)} = \frac{d}{dt}\log(\epsilon + u(t)), \tag{2}$$

where ϵ is a small bias term that avoids division by zero. We also computed the correlation between transient responses and concentration contrast and found that PN transient responses show a significiantly higher correlation with concentration contrast than OSNs (see **Fig.**2(D middle)).

As *concentration invariance* and *contrast boosting* capture both steady-state and transient response characteristics that differentiate PN from OSN PSTHs, they serve as important metrics in evaluating model circuits of the Antennal Lobe. In the following section, we systematically compare models of temporal processing in the Antennal Lobe, seeking circuits with low concentration dependency (low correlation between steady-state response and concentration waveform) and high contrast boosting (high correlation between transient response and concentration contrast). Since odorant waveforms are represented in steady-state ($[\mathbf{b}]_{ron}/[\mathbf{d}]_{ron} \cdot u(t)$) and transient states ($[\mathbf{d}]_{ron}$) by the OSN PSTH, the comparison of AL model circuits will need to address the central question of temporal odorant processing in the AL: determining the circuit architecture that enables 1) decoupling of affinity and concentration of PN steady-state responses and 2) boosting the PN transient response levels.

2.2 Presynaptic and Postsynaptic Local Neurons Enable Concentration Invariance and Contrast Boosting in Temporal Processing of Single Channels

To systematically investigate the functional logic of the Antennal Lobe, we exhaustively compared all variations of AL circuits involving the three aforementioned local neuron types: 1) inhibitory Pre-LNs, 2) excitatory Post-eLNs, and 3) inhibitory Post-iLNs. From an architectural perspective, we compare, on the pre-synaptic side of the OSN-to-PN synapse, three different configurations of Pre-LN inhibition of the OSN Axon-Terminal: 1) no Pre-LNs (Baseline Circuit, **Fig.**3(A[i])), 2) Pre-LN receiving input from the OSN Axon-Terminal and inhibiting the OSN Axon-Terminal (Local Feedback Circuit, **Fig.**3(A[ii])), and 3) Pre-LNs receiving input from the OSN Axon-Hillock and inhibiting the OSN Axon-Terminal (Local Feedforward Circuit, **Fig.**3(A[iii])). On the post-synaptic side of the OSN-to-PN synapse, we consider three configurations of Post-eLNs and Post-iLNs: 1) no Post-eLNs or Post-iLNs (Baseline Circuit, **Fig.**3(A[i])), 2) only Post-eLNs (**Fig.**3(A[iv])), 3) only Post-iLNs(**Fig.**3(A[v])), 4) both Post-eLNs and Post-iLNs (**Fig.**3(A[vi])). Combining both pre-synaptic and post-synaptic configurations, we have a total of 12 circuit architectures, 8 of which are shown in **Fig.**3.

In addition to the topology of the architecture, full specification of each circuit re-

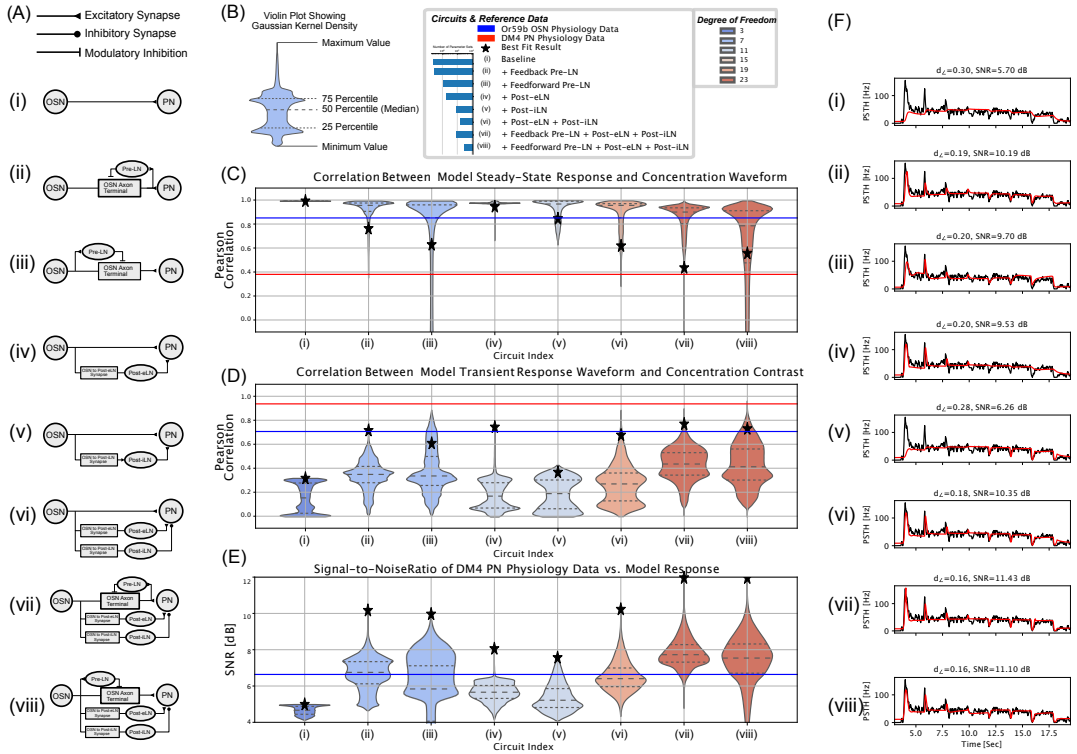

Figure 3: Best fit SNR and distribution comparisons between temporal odor signal processing of single channel circuit architectures (Or59b OSN and DM4 glomerulus). (A) Circuit architectures. (B) Reference for violinplot, legend for model and color reference for degree of freedom (number of free parameters) of each model. (C) Sample distribution of the correlation between the steady-state responses and concentration waveform over the parameter space for each of the 8 models. The correlations between the steady-state response and the concentration waveform for DM4 PN and Or59b OSN physiology data are shown, for reference, in red and blue lines, respectively. (D) Sample distribution of correlation between the transient responses and concentration contrast over the parameter space for each of the 8 models. The correlations between the steady-state response and the concentration waveform for DM4 PN and Or59b OSN physiology data are shown, for reference, as red and blue lines, respectively. (E) Sample distribution of Signal-to-Noise Ratio between physiology recording data of DM4 PN and model responses. For reference, the Or59b OSN physiology data is linearly scaled to achieve the best SNR against the DM4 PN physiology data. The SNR between the scaled OSN response and PN response is shown in blue. (F) Responses of best fit models. Other metrics associated with the best fit results are shown as black stars in (C-F).

quires model definition and parameterization of individual components. From the modeling perspective, we looked at the Calcium Feedback Loop of the Odorant Transduction Process (OTP, [2]) model for inspiration, which produces a similar, tough much weaker, transient response as that observed in the PN physiology data (see **Fig.**2(D middle row)). We modeled the Pre-LN inhibition of the OSN Axon-Terminal similar to the inhibition exerted by the calcium channel in the OTP. Here the spike train of Pre-LN multiplicatively inhibits the neurotransmitter release of the OSN Axon Terminal (see Methods for details). The OSN-to-PostLN synapse

Model Index	(i)	(ii)	(iii)	(iv)	(v)	(vi)	(vii)	(viii)
SNR [dB]	5.7	10.19	9.7	9.53	6.26	10.35	11.43	11.10
Ranking by SNR	8	4	5	6	7	3	1	2
Odorant Transient Captured	N.A.	ON & OFF	ON & OFF	ON	OFF	ON & OFF	ON & OFF	ON & OFF

Table 1: Comparison of best fit results of each temporal circuits in **Fig.**3(B).

model expands upon the calcium feedback loop to provide the flexibility to strongly respond to either input onset and offset based on parameter choice. Finally, all other synapse models are assumed to be ionotropic and all biophysical spike generators noisy Connor-Stevens point neurons (see [2] and Methods). Together, the combined number of parameters for all components determine the degree of freedom of each circuit, an example of which is shown in **Table.**2.

Given full circuit specifications (architecture and model parametrizations), we sought to optimize the parameters of each circuit by minimizing the L_2 distance between the temporal response of the circuit PSTH and the DM4 PN PSTH from physiology recordings. Due to the high number of parameters for the more complex circuits (e.g., 24 in the most complex circuit), we utilized a 2-step optimization procedure (see **Section** 4.5) that combines an initial random sampling of the parameter space and a fine-tuning global optimization step. The temporal response of the circuit models with the lowest L_2 distances (best fit) are shown in **Fig.**3(F) (see **Fig.**8 for results of all 12 models).

In addition to determining the best-fit circuits via the 2-step optimization procedure, we also sought a global view of the objective function landscape of the circuit models. Such global perspective enables comparison between the functional capabilities inherent in the topology of the architecture, rather than a specific parameterization. To that end, for each circuit, we randomly sampled at least 10^6 parameters, and stimulated in excess of 5×10^8 circuit/parameter combinations. Collecting results from each parameter choice, we computed the sample distribution of the SNR for all circuits, each drawn as a violin-plot in **Fig.**3(E) (see **Fig.**3(B left) for an explanation of the violin-plots. Note that that circuit name and circuit degree of freedom are detailed in the legends in **Fig.**3(B). Additionally, we computed the sample distributions of the correlation between the steady-state response and concentration waveform (**Fig.**3(C)), and the transient response and concentration contrast (**Fig.**3(D)). For reference, the same procedure is repeated for DM4 PN PSTH and Or59b PSTH, and the resulting correlation values are shown in red and blue in **Fig.**3(C,D), respectively.

Referencing the results in **Fig.**3(F), we first compared the best fit results of each

circuit in terms of 1) the Signal-to-Noise Ratio (SNR) between circuit response and the PN physiology data and 2) the contrast boosting performance in terms of the response amplitudes to positive and negative concentration contrasts. Referencing the result of the comparison summarized in **Table.**1, we note that:

- the Baseline circuit (model (i)), with no LNs, results in the lowest SNR, and fails to respond to On/Off odorant transients;
- the addition of Post-eLN (in model (iv)) improves the SNR significantly by 3.83 dB above that obtained with the baseline circuit and captures the odorant onset transient;
- the addition of Post-iLN (in model (v)) improves the SNR moderately by .56 dB above that obtained with the baseline circuit and captures the odorant offset transient;
- the addition of Pre-LN (in either feedback or feedforward configurations in model (ii) or (iii)) significantly improves the SNR (by 4.49 dB and 4 dB, respectively), and captures both the onset and offset odorant transients.

Next, we compared the sample distributions shown in **Fig.**3(C-D), particularly the median as well as the 25/75 quantiles indicated as horizontal dashed lines within each violin-plot. Note that, for each circuit architecture, the correlations of the best fit results are marked with black stars in **Fig.**3(C-D). From **Fig.**3(E), we observe that the median SNR across parameterizations of each circuit follows the ranking of the best fit results shown in **Table.**1. We observe that, models (ii-iii) achieve significantly higher SNR across parameterization than models (iv-v), and are comparable to the SNR achieved by model (vi). This indicates that the Pre-LN is critical in capturing the PN overall temporal response, while the simultaneous introduction of Post-eLN and Post-iLN is necessary to significantly improve the circuit's odor signal processing capability. On the other hand, the combination of both pre-synaptic and post-synaptic LNs resulted in the highest overall SNR. These observations are supported in **Fig.**3(C2), where the level of concentration-invariance is comparable between circuit (ii, iii) and circuit (vi), while a significant portion of parametrizations of circuit (vii, viii) lead to a concentration dependency level similar to that observed in the PN data. Similarly, in **Fig.**3(C3), circuits (ii,iii) consistently out-perform (iv,v) in capturing the concentration contrast during transient response, and are comparable to the combined Post-eLN+Post-iLN circuit in (vi). As before, the model with the highest degree of complexity, circuits (vii, viii) show the best contrast-encoding capabilities according to both the highest median as well as 75 percent quantile values, with the maximum correlation of model (viii) reaching the level observed in the PN data.

In conclusion, we have demonstrated that for the single channel temporal response of the Antennal Lobe circuit, the addition of a presynaptic local neuron (Pre-LN) significantly improves both concentration invariance and contrast boosting for both feedback and feedforward circuit configurations. Moreover, the introduction of both Post-eLN and Post-iLN is required for contrast boosting. The Post-LNs can further boost the contrast at the output of the Pre-LNs circuits without sacrificing on concentration-invariance.

2.3 Spatio-Temporal Processing of Odorant Waveforms

Similar to comparison between the models of temporal processing in the previous section, we exhaustively compared spatio-temporal models of the AL circuit that are differentiated by their innervation patterns on both the presynaptic and postsynaptic sides of the OSN-to-PN synapse. On the presynaptic side, we consider 5 circuit architectures with: 1) no Pre-LNs **Fig.**4(A[i]), 2) Pre-LNs innervating individual glomeruli in feedback or feedforward configurations **Fig.**4(A[ii,iii]), and 3) Pre-LNs innervating all glomeruli in feedback or feedforward configurations **Fig.**4(A[vi,vii]). On the postsynaptic side, the addition of Post-eLNs and Post-iLNs to circuits with local Pre-LN inhibitions result in models in **Fig.**4(A[iv,v]), and likewise for circuits with global Pre-LN in **Fig.**4(A[viii, ix]). Three additional configurations of Post-LNs were also explored (No Post-LNs, only Post-eLNs, only Post-iLNs). Hence, combining all configurations of presynaptic and postsynaptic connectivites, we compared a total of 20 different spatio-temporal circuit architectures, 9 of which are shown in **Fig.**4(A) (see **Fig.**10 for comparison between all 20 models.)

To reduce the total degrees of freedom, models describing the same circuit components across channels share the same parameter values. As such, the total degrees of freedom for the spatio-temporal circuits is the same as that of their temporal counterparts. For circuits with global Pre-LN inhibition, e.g., Global-Feedforward in **Fig.**4(A[vii]), all OSN-to-PreLN synapses share the same parameter values, and the dendritic process of the Pre-LNs was modeled as the linear sum of synaptic currents across all synapses. As no additional parameters were introduced, the Global-Feedforward circuit has the same degree of freedom as the Local-Feedforward circuit.

From an optimization standpoint, beyond minizing the L_2 distance between DM4 PN PSTHs of circuit models and physiology recordings, we introduced an additional objective that sought to minimize the distance between PN steady-state response vectors and the odorant affinity vector. The additional objective is motivated by

the hypothesis that the concentration-invariance of the PN response is a single-channel manifestation that extends across all AL channels. As the odorant identity is represented by the affinity vector in steady-state, the objective is the angular distance between the PN steady-state response and the odorant affinity vector. The latter is minimized when the two vectors are, up to a scaling factor, identical.

Finally, the multi-objective optimization problem minimizes the sum of the two objectives with a weighting factor $\lambda > 0$ (see Methods for details), where $\lambda = 0$ results in the same objective for the temporal circuits (see **Fig.**11 for the influence of λ on the DM4 PN PSTH produced by the circuits.) In **Fig.**4, we chose $\lambda = 5$ and applied the same 2-step optmization procedure and random sampling of parameter spaces as before.

We begin by comparing the SNR of DM4 PN PSTH obtained by temporal circuits in **Fig.**3(E[i,ii,iii,vii,viii]) and their parallel processing spatio-temporal counterparts in **Fig.**4(E[i,ii,iii,iv,v]). We note that, as expected, the parallel processing spatio-temporal circuits achieve very similar SNRs as their temporal counterparts. Such similarity is also observed by comparing the correlations for steady-state and transient PN responses in **Fig.**4(C[i,ii,iii,iv,v]) and **Fig.**4(D[i,ii,iii,iv,v]).

Comparing the angular distances between PN steady-state responses and the affinity vectors for the parallel processing circuits shown in **Fig.**4(F[i,ii,iii,iv,v]), we note that the Local-FF and Local-FB circuits exhibit some, albeit limited improvement over the baseline with the lowest angular distance achieved by the Local-FF model at 0.18 as compared to 0.2 for the baseline circuits. The addition of Post-LNs in **Fig.**4(F[iv,v]) resulted in a similar improvement in odorant recovery performance.

However, as shown in **Fig.**4(F[vi, vii]), circuits with global inhibition from Pre-LN (Global Feedback, Global Feedforward) show drastic improvement of odorant recovery as compared to their circuits with local Pre-LN inhibition, without a significant decrease in the overall SNR along the DM4 channel (see **Fig.**4(E[vi, vii])). Notably, the contrast boosting capability of the Global Feedback model is greatly reduced from its local counterpart as shown in **Fig.**4(D[vi]). The addition of Post-LNs, as shown in **Fig.**4(D[viii]), leads to an improvement.

In addition to optimizing the model to recover the Acetone affinity vector, we further evaluated, across a range of concentration values, the ability of the best fitted circuits to recover the identities of 110 odorants with known affinity vectors [2, 25]. This was achieved by stimulating each spatio-temporal circuit using step concentration waveforms with an amplitude ranging from 10 ppm to 1,000 ppm, and comparing the steady-state PN responses to the affinity vectors of each odorant. The resulting

distances are shown in **Fig.**5(B) as heatmaps. Here each row corresponds to a specific concentration level (in log scale), and each column corresponds to an odorant identity. Note that, across circuits, for each odorant (along each column), the angular distance is highest (indicating worst recovery) at very low/high concentration levels, and is lowest at intermediate concentration levels. We also present the histograms of angular distances in heatmaps in **Fig.**5(B) as violin plots in **Fig.**5(D). The results depicted clearly show that the Global Feedback and Global Feedforward models achieve significantly better odorant recovery than the other models. Finally, to isolate the computation performed by the Antennal Lobe from that by the Antenna, we plotted the angular distance between (PN steady-state response, affinity vectors) versus (OSN steady-state response, affinity vectors) in **Fig.**5(C). Since the degree of odorant recovery is inversely proportional to the angular distance, an *improvement* from Antenna response would by reflected in **Fig.**5(C) as data below the diagonal line. Importantly, as shown in **Fig.**5(C[iv, v]), the global inhibition models show an uniform improvement of odorant identity recovery, with minimum angular distances reaching 0, indicating perfect odorant identity recovery. Circuits with local Pre-LN inhibition, on the other hand, do not show such uniform improvement of odorant recovery (**Fig.**5(C[i-iii]).

Similarly, we sought to evaluate the robustness of the transient response to concentration level and contrast changes. For 3 odorant waveforms with different concentration contrasts (step, ramp, parabola, **Fig.**6(A1,B1,C1)), we measured the Post-eLN and Post-iLN responses in the DM4 channel. As shown in **Fig.**6(A2), for step acetone odorant waveform of concentrations ranging from 1 to 10,000 ppm, the Post-eLNs fire reliably at the odorant onset of 6 seconds, while the Post-iLNs fire reliably at the odorant offset at 9 seconds. Quantitatively, we measured the peak Post-eLN and Post-iLN spike rate during the 5-10 seconds window, as well as the timing of the peak Post-eLN and Post-iLN responses. The results are shown in **Fig.**6(A3). As depicted in **Fig.**6(A3, left), the peak Post-eLN (shown in red) and Post-iLN (shown in blue) spike rates remains relatively constant for input concentration amplitude values above 2,000 ppm, while the OSN spike rate (shown in black) increased by almost 50% from $\sim$ 150Hz at 2,000 ppm to around $\sim$ 220 Hz at 10,000 ppm. In addition to the stable response amplitude, the timing of the peak responses is remarkably consistent across concentration levels as shown in **Fig.**6(A3, right), indicating that the Post-LNs provide ON/OFF timing information regardless of input concentration levels. Since the PN transient responses reflect the concentration contrast, the Post-LN responses to odorant ramp and parabola waveforms, with a significantly lower contrast level, are lower than that of the step waveforms. Nevertheless, Post-LNs are able to respond to ramp input onsets/offsets reliably with an input amplitude above 1,000

ppm (**Fig.**6(B3)), and to parabolic input at levels above 4,000 ppm (**Fig.**6(C3)). Therefore, the Post-LNs are shown here to be able to facilitate contrast boosting of the AL circuits with global Pre-LN inhibition across odorant concentration levels.

In conclusion, by extending the temporal models to their spatio-temporal counterparts, and introducing models with global Pre-LN inhibition, we have shown that odorant identity recovery requires global Pre-LN inhibition. Additionally, we have shown that models with global Pre-LN inhibition exhibit similar temporal responses along the DM4 channel, suggesting that the improvement in odorant recovery obtained by changing local inhibition to global inhibition does not lead to a significant decrease in temporal processing performance of the circuits. Finally, we have shown that Post-LN responses are robust to change in concentration levels, thereby facilitating contrast boosting of Pre-LN circuits across odorant intensity values.

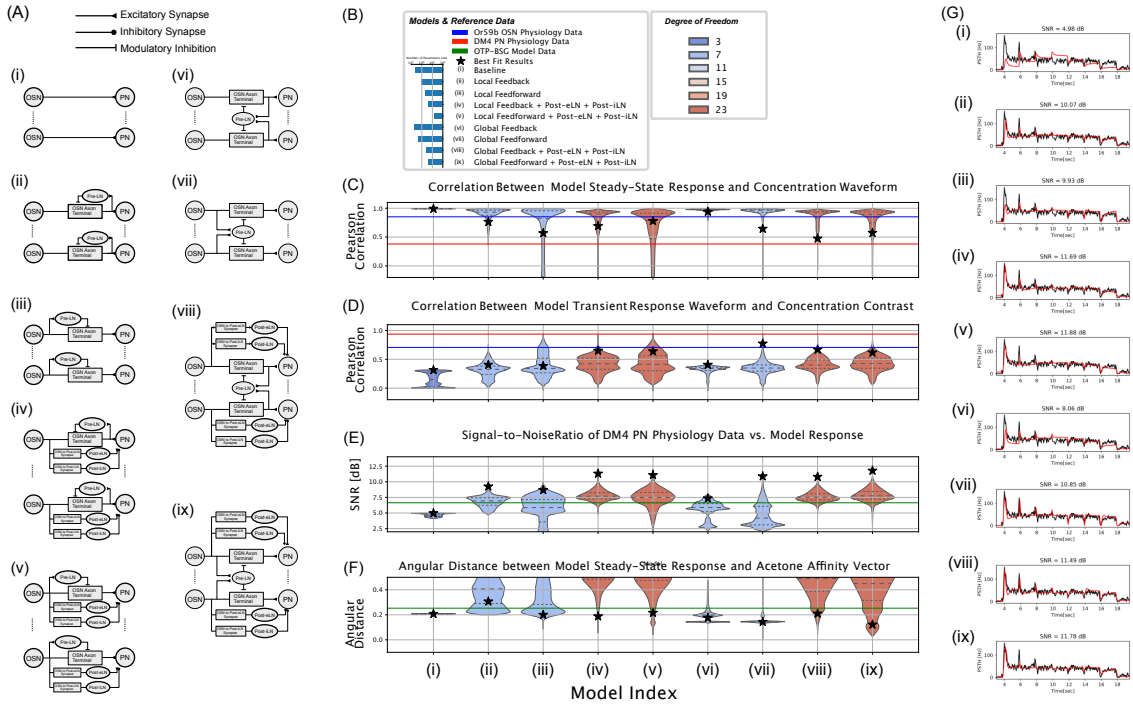

Figure 4: Global Feedforward/Feedback models of Antennal Lobe out perform Local Feedforward/Feedback models across parameterization. (A) Circuit architectures. (B) Legend for model and degree of freedom. (C) Correlation between spatio-temporal model steady-state response in DM4 channel to staircase Acetone stimulus and concentration waveform. (D) Correlation between spatio-temporal model transient response in DM4 channel to staircase Acetone stimulus and concentration contrast. (E) Signal-to-Noise ratio between spatio-temporal model response in DM4 channel to staircase Acetone stimulus and physiology data. The distance between steady-state response of the OTP-BSG model and Acetone odorant affinity vector is shown in green for reference. (F) Average distance between spatio-temporal model responses and Acetone odorant affinity vector. The distance between steady-state response of the OTP-BSG model and Acetone odorant affinity vector is shown in green for reference. (G) DM4 PN PSTH of best fit results of each circuit. Other metrics associated with the best fit results are shown as black stars in (C-F).

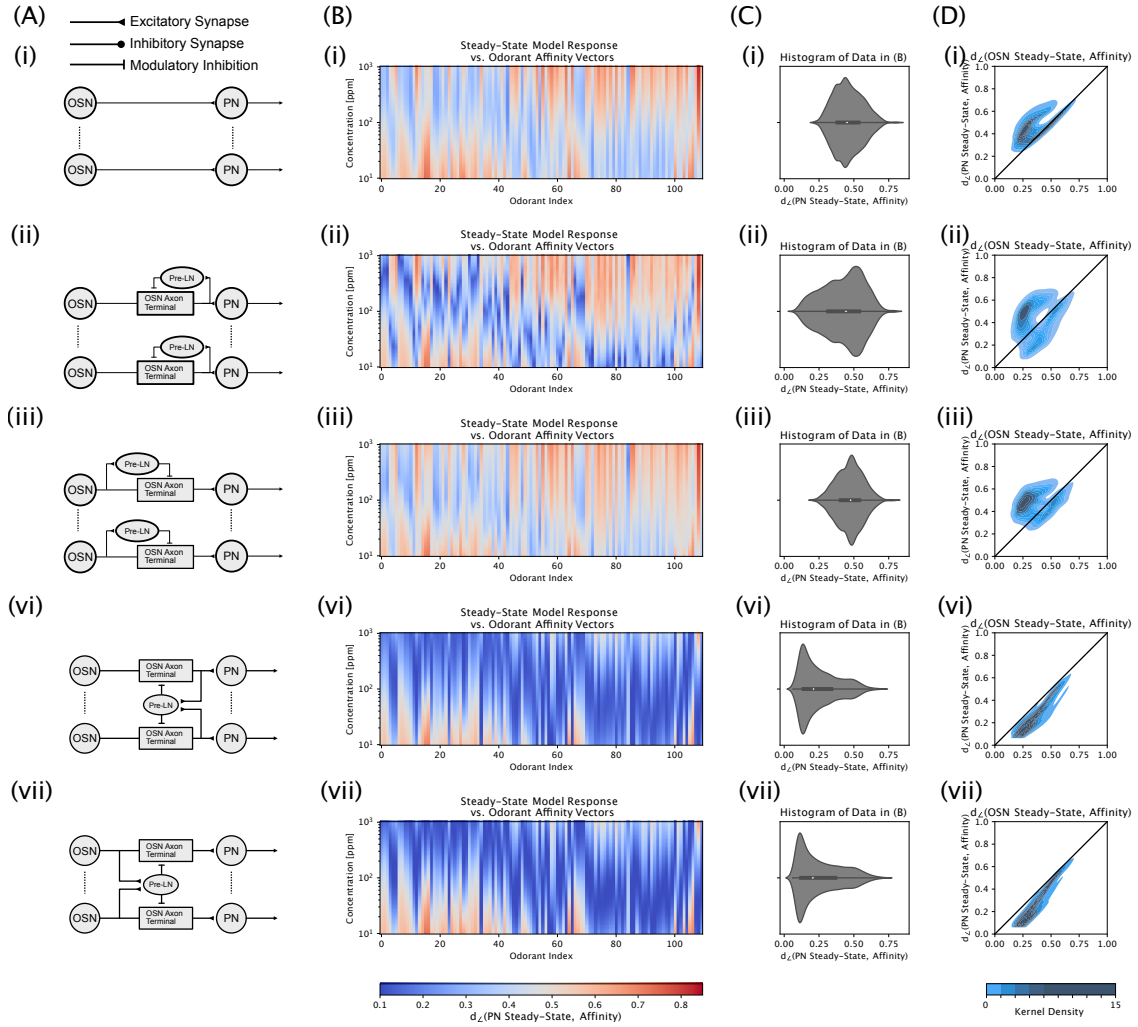

Figure 5: Recovery of mono-molecular odorant identities by spatio-temporal response of the Antennal Lobe for 110 odorants with known estimated affinities across concentration levels. 5 models of the spatio-temporal processing of tspahe Antennal Lobe is considered for the odorant identity reconstruction evaluation, each shown as a row indexed [i] to [v]. For each model (row), the figures (column) indicate: (A) Illustration of models; (B) Angular distance between model steady-state responses and affinity vectors for 110 odorants at $10 \sim 1000$ $[ppm]$ concentration levels. (C) Histogram of data in (B) presented as violin-plots. (D) Comparison of data in (B) vs. angular distance between steady-state response of OSNs and affinity vectors (data not shown) presented as heatmap estimated using 2D kernel density estimation with gaussian kernel. Note that data below the diagonal line indicates a reduction of angular distance between model response and affinity vector over the OSN response, vice versa.

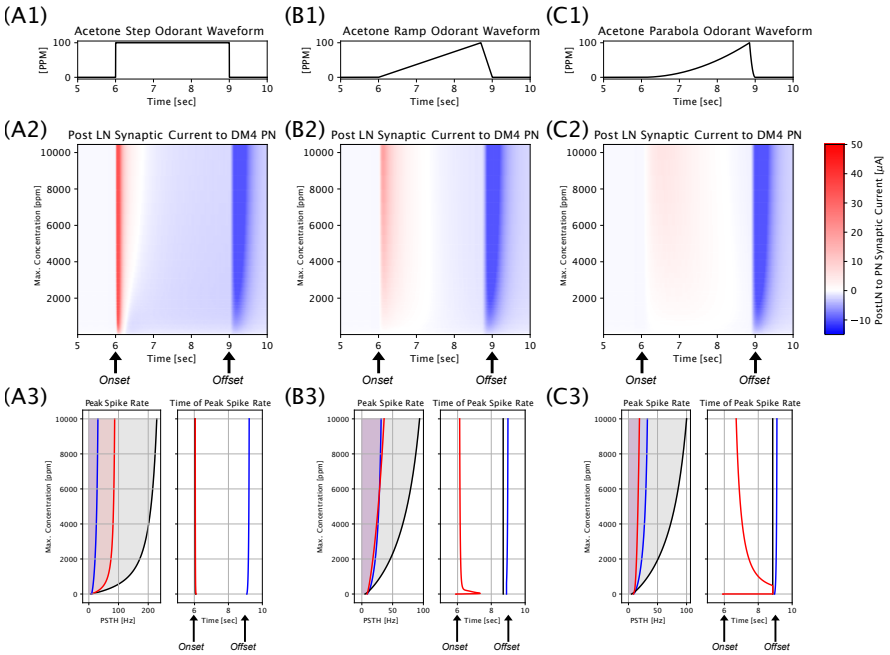

Figure 6: Postsynaptic Local Neurons (PostLNs) robustly encode odorant on/off-set timing information. (A1) Step Acetone waveform input to OSNs. (A2) Synaptic current from Post-eLN and Post-iLN to DM4 PN across concentration levels from 1 to 10^4 ppm for step concentration waveform. Excitatory input is shown in red and Inhibitory input is shown in blue. (A3) Amplitude and timing of the peak Post-eLN (red) and Post-iLN (blue) responses in comparison to OSN (black). (B1-B3) Same as (A1-A3) for ramp concentration waveform with smaller onset/offset concentration contrast. (C1-C3) Same as (A1-A3) for parabola concentration waveform with the smallest onset/offset concentration contrast.

3 Discussion

In complex olfactory environments, *Drosophila* need to rapidly and robustly identify and react to changing odorant identities. Focusing on spatio-temporal response to mono-molecular odorant input at the level of the Antennal Lobe, we extensively compared circuit architectures involving different configurations of Local Neuron connectivity patterns. We have shown that the diverse set of LNs recover odorant identity information from the OSN spike trains, and contribute to the strong odorant onset and offset transient responses.

Odorant Encoding in the Antennal Lobe The encoding of odorants is characterized by the multiplicative coupling between the odorant identity (binding and dissociation rates) and concentration [2]. The encoding process leads to a confounding representation of odorant identity and concentration [7, 8]. Analysis of OSN and PN physiology data suggest that the PN response exhibits concentration invariance and contrast boosting properties, thereby decoupling odorant identity from concentration information in steady-state while responding strongly to odorant onset and offset in transient states.

Circuit Architectures of the Antennal Lobe Connectome of adult [22] and larva [23] *Drosophila* AL has revealed that glomeruli in the AL are innervated by a wide variety of Local Neurons (LNs) characterized by their connectivity patterns and neurotransmitter profiles. Here, we focused on three main LN cell types: 1) inhibitory pre-synaptic (to OSN-to-PN synapse) LN (Pre-LN) that innervate all glomeruli, 2) inhibitory (Post-iLN) and 3) excitatory (Post-eLN) post-synaptic (to OSN-to-PN synapse) LNs that innervate single/few glomeruli. For completeness, we compared all combinations of LN connectivity patterns (LN types, local vs. global, and feedforward vs. feedback) for either temporal (single channel) or spatio-temporal (multi-channels) odor signal processing in the AL. The extensive comparison allowed us to isolate the computational roles and capabilities of individual LNs.

Optimizing Connectome-Constrained Model of the AL The evaluation of a large number of circuits is only possible via massively parallel simulation on Graphical Processing Units (GPUs) [26, 27]. Furthermore, for each circuit configuration, we computed empirical distributions of identity recovery across randomly sampled parameters, providing insights into the computational capabilities of model structures, rather than specific parameterizations of said models.

For temporal processing of odorant input along a single channel, we found that, in the absence of Local Neurons, OSN-to-PN cholinergic synapses (baseline model) are unable to capture the concentration-invariance and contrast-boosting properties observed in the DM4 PN physiology data. While inhibition from Pre-LN can reduce concentration-dependency of the steady-state PN response, it alone cannot reliably encode odorant concentration contrast across parameterizations. On the other hand, Post-eLN and Post-iLN enhances the contrast-boosting for not only the Local-FF and Local-FB but also the baseline model across all parameterizations.

For spatio-temporal processing of mono-molecular odorants, we found that inter-glomeruli communication with Pre-LN connecting globally to all glomeruli (in either feedback (Global-FB) or feedforward (Global-FF) configurations) is necessary to reconstruct the odorant affinity vector at the level of the PNs. Furthermore, while Post-eLNs/Post-iLNs connect locally within each glomerulus, they respond robustly to odorant onsets and offsets. As such, Post-LNs' excitations/inhibitions to PNs act as event detectors that indicate changing odorant identity. Together with the odorant identity recovery achieved by global Pre-LN inhibition, we have shown that the AL implements an event-based odorant identity recovery processing scheme for rapid and robust processing in downstream neuropils.

We note that by recovering the odorant affinity vector, AL responses also disambiguate between different odorant stimuli, consistent with observations made by previous studies investigating a small subset of glomeruli [28, 29, 30, 31].

Methodology We note that neural circuits are highly nonlinear dynamical systems. As such, theoretical analyses, though helpful in providing intuition, are often insufficient to predict model behavior even with gross approximations. On the other hand, experimental explorations are essential in providing ground truth data, are often limited to a small subset of the complete neural circuit. With the rapid development of Graphic Processing Units (GPUs), massively parallel computational exploration has made comparison between all circuit configurations across parameterizations possible. Such capabilities have enabled us to analyze realistic models of neural circuits that reflect the complexity of both the connectome and the processing within individual circuit components, and is essential in bridging the gap between brain structure and function.

Experimental Verification and Future Works As the odorant identity is characterized by the PN spatio-temporal population response, experimental verification of our models require simultaneous PN recordings for all glomeruli. For example,

while the temporal response of DM4 PN was verified against physilogy data, the evaluation of the spatio-temporal AL response can only be obtained by comparing it against odorant affinity vectors, and not physiology recordings. Biological verification of the spaio-temporal model, therefore, requires systematic characterization of population PN responses.

From a modeling standpoint, we note that choices of individual components are not unique. For example, the OSN-to-PostLN synapse model presented here captures either the odorant onset and offset transients. However, similar behavior can also be achieved by two distinctive models of OSN-to-Post-eLN and OSN-to-Post-iLN synapses, each capturing odorant onset and offset respectively. Although we opted to describe the OSN-to-PostLN synapse with a single model with a relatively high number of parameters, such choice remains to be validated by additional biological insight into the diversity of OSN-to-PostLN synapses.

Additionally, while the AL models compared are exhaustive for the LN cell types considered, they do not capture the full complexity of the Antennal Lobe. For example, the AL processing paradigm considered here assumes that the population response of the uni-glomerular PNs recover the odorant identity, without a need to account for the multi-glomerular PNs. Additionally, the LN cell types are assumed to be either pan-glomerular or uni-glomerular, while many LNs in the AL fall in between the two extremes. Nevertheless, the models presented herein can be readily extended to incorporate the additional neuron types.

4 Materials and Methods

4.1 Decomposing OSN and PN responses into steady-state and transient components

For odorant concentration waveforms that are piecewise constant (e.g., step, staircase), we linearly decomposed the neuron response PSTH into steady-state and transient components using the following steps (see **Fig.**2(C2) for example):

- *Extracting odorant waveform jump times*: we first computed the odorant contrast using **Eq.**(2) with $\varepsilon = 1$, and stored the time of the peak values of the odorant concentration contrast as jump times.
- *Computing steady-state component*: we then created a piecewise constant steady-state response with transition times specified by the jump times, and the am-

plitude specified by the average response during the 500 milisecond prior to each jump time.

- *Computing transient component*: the transient response is the residual of subtracting the steady-state response from the overall response.

4.2 Metrics

Square-Integrable Functions and L^2 Norm The concentration waveforms and output PSTHs considered in the current work are assumed to be in the space of square-integrable functions (not necessarily bandlimited). For such signals, we respectively use L^2 norm and the uniquely defined inner-product

$$\|u(t)\|_{L^2} = \sqrt{\int_{\mathbb{R}} |u(t)|^2 dt}, \qquad \langle u, v\rangle_{L^2} = \int_{\mathbb{R}} u(t)v(t)dt.$$

Signal-to-Noise Ratio For a clean signal $u(t)$ and the noisy signal $\tilde{u}(t) = u(t) + n(t)$ where $n(t)$ is the noise, the SNR is given (in deciBel) as

$$SNR(u, n) = 10 \log_{10} \left[\frac{\|u(t)\|^2_{L^2}}{\|u(t) - \tilde{u}(t)\|^2_{L^2}} \right].$$

(Maximum) Cross-Correlation Consider two signals $u(t), v(t)$ with temporal support $[T_1, T_2]$. The Cross-Correlation is measured as:

$$Corr(u(t), v(t)) = \frac{\langle u - \mu_u, v - \mu_v\rangle_{L^2}}{\|u - \mu_u\|_{L^2}\|v - \mu_v\|_{L^2}},$$

where $\mu_u = \frac{1}{T_2 - T_1}\int_{T_1}^{T_2} u(t)dt, \mu_v = \frac{1}{T_2 - T_1}\int_{T_1}^{T_2} v(t)dt$ are, respectively, the average value of the signals. To account for delay between signals $u(t), v(t)$, Maximum Cross-Correlation can be used to robustly measure the similarity between the two signals, given as:

$$Corr_{max}(u(t), v(t)) = \max_{\tau} Corr(u(t), v(t - \tau)).$$

Angular Distance Although the cross-correlation is a scale-invariant measure of similarity between signals, it is not a proper metric since it violates the triangular inequality [32]. A related pseudo-metric that is heavily used in the current work is the angular distance, defined as:

$$d_{\angle}(u, v) = \frac{2 \cdot \arccos(1 - d_{\cos}(u, v))}{\pi} \in [0, 1],$$

where $d_{\cos}$ is the cosine distance given as:

$$d_{\cos}(u, v) = 1 - \frac{\langle u, v \rangle}{\|u\|\|v\|} \in [0, 1].$$

4.3 Biophysical Models and Parameterizations

Ionotropic Synapse

All excitatory and inhibitory synapses are described by an ionotropic synapse model. For input signal $u(t)$, the normalized conductance x and the synaptic currents I are given as:

$$\begin{aligned} \frac{dx}{dt} &= \alpha_1 \cdot u(t) \cdot (1 - x) - \beta_1 \cdot x \\ I &= \overline{g}_{max} \cdot x \cdot (V_{post} - E_{rev}), \end{aligned} \tag{3}$$

where α_1, β_1 are the rate constants of the synapse dynamics, $\overline{g}_{max}$ is the maximum conductance value, E_{rev} is the reversal potential of the synapse and V_{post} is the membrane potential of the postsynaptic neuron. The reversal potential was set to $0mV$ for excitatory synapses and $-100mV$ for inhibitory synapses.

Note that the input signal $u(t)$ can either be the spike train $\sum_k \delta(t - t_k)$ (e.g., OSN to Pre-LN synapse) or the neurotransmitter concentration $[NT](t)$ (e.g., for the OSN Axon-Terminal).

Number of free parameters for the ionotropic synapse is 3: $\theta = [\alpha_1, \beta_1, \overline{g}_{max}]$.

OSN Axon-Terminal

The model of OSN axon-terminal takes the $\sum_k \delta(t - t_k^O)$ and the Pre-LN spike train $\sum_k \delta(t - t_k^L)$ as inputs, and outputs the neurotransmitter concentration $[NT](t)$:

$$\begin{aligned} \frac{dx_1}{dt} &= \alpha_1 \cdot \sum_k \delta(t - t_k^O) \cdot (1 - x_1) - \beta_1 \cdot x_1 - \kappa \cdot \sum_k \delta(t - t_k^L) \cdot x_1 \\ [NT](t) &= [NT]_{max} \cdot x_1(t) \end{aligned}, \tag{4}$$

where α_1, β_1 are rate constants, κ is the inhibition constant, and $[NT]_{max}$ is the maximum neurotransmitter concentration. The neurotransmitter concentration, in turn, drives the OSN-to-PN ionotropic synapse described by **Eq.**(3).

Number of free parameters for the OSN Axon-Terminal is 4: $\theta = [\alpha_1, \beta_1, \kappa, [NT]_{max}]$.

OSN-to-PostLN Synapse

The OSN-to-PostLN Synapse takes the OSN spike train $\sum_k \delta(t - t_k^O)$ as input and outputs the synaptic current I, governed by the set of equations:

$$\begin{aligned} \dot{x}_1 &= \alpha_1 \cdot x_2 \cdot (1 - x_1) - \beta_1 \cdot x_1 - \kappa \cdot x_3 \cdot x_1 \\ \dot{x}_2 &= \alpha_2 \cdot \sum_k \delta(t - t_k^O) \cdot (1 - x_2) - \beta_2 \cdot x_2 \\ \dot{x}_3 &= \alpha_3 \cdot \sum_k \delta(t - t_k^O) \cdot (1 - x_3) - \beta_3 \cdot x_3 \\ I &= \overline{g}_{max} \cdot x_1 \cdot (V^L - E_{rev}), \end{aligned} \quad , \tag{5}$$

where $\alpha_1, \beta_1, \alpha_2, \beta_2, \alpha_3, \beta_3$ are rate constants, κ is the inhibition constant, $\overline{g}_{max}$ is the maximum conductance, V^L is the membrane potential of Post-eLN/Post-iLN, and E_{rev} is the reversal potential.

As OSN is cholinergic, we assume that the OSN-to-PostLN synapses are all excitatory, i.e., $E_{rev} = 0\ mV$.

Number of free parameters for the OSN-to-PostLN synapse is 8: $\theta = [\alpha_1, \beta_1, \alpha_2, \beta_2, \alpha_3, \beta_3, \kappa, \overline{g}_{max}]$.

Biophysical Spike Generator (Axon-Hillock)

Following [2], the axon hillocks of all neuron models are described by a noisy Connor-Stevens neuron model. The noise levels of the neuron models are chosen such that OSNs have a resting spike rate of 8 Hz, Local Neurons (Pre-LN, Post-eLNs, Post-iLNs) have a resting spike rate of 0 Hz, and Projection Neurons have a resting spike rate of 1 Hz (see **Fig.**7 for reference of the impact of noise standard deviation on the Frequency-Current curve of the noisy Connor-Stevens model). We note that the noise parameter is not tuned extensively and other choices of noise standard deviations are also possible (e.g., noise parameter that leads to resting spike rate of 1 Hz for PNs).

Number of free parameters for the Biophysical Spike Generator synapse is 0.

4.4 Optimization Objectives

Temporal Models

For temporal models presented in **Section** 2.2, we sought to minimize the distance between PN spike rate of the models parameterized by θ ($\tilde{r}^P(t;\theta)$) and physiology

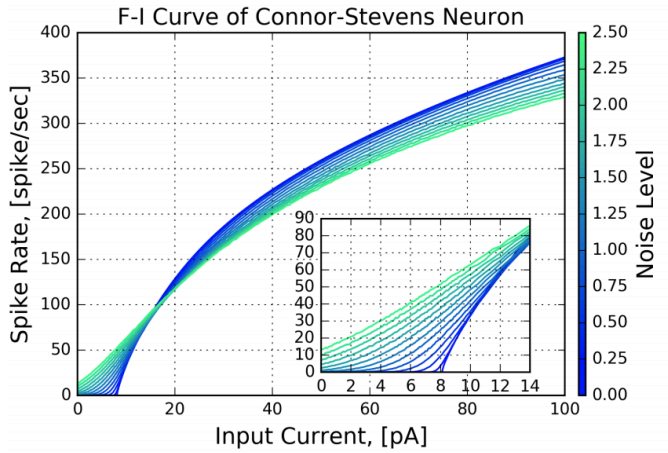

Figure 7: Frequency-Current curve of the Noisy Connor-Stevens neuron model.

response $r^P(t)$:

$$\begin{aligned} \min_{\theta \in \mathbb{R}^3_+} \quad & \underbrace{\|\tilde{r}^P(t;\theta) - r^P(t)\|_{L^2}}_{J_1(\theta)}, \\ \text{s.t.} \quad & \max_t x(t) < 0.8 \end{aligned} \tag{6}$$

where $x(t)$ indicates the normalized synaptic conductance of the OSN Axon-Terminal (or normalized conductance of OSN-to-PN synapse for "Baseline" models)

We note that all models of the Antennal Lobe are built upon Kinetic Models that exhibit saturation at normalized value 1 for high input levels. At this saturation regime, the model would seemingly exhibit *Concentration Invariance* as any non-zero concentration value will lead to saturation at the limit. The inequality constraint in **Eq.**(6) is a heuristic to keep the normalized synaptic conductance x below saturation level, and to ensure that the *Concentration Invariance* is not the artifact of model saturation, but rather achieved via the model structure.

Spatio-Temporal Models

For Spatio-Temporal models of the Antennal Lobe, the overall optimization objective is described as:

$$\begin{aligned} \min_{\theta} \quad & \underbrace{\|\tilde{r}^P(t;\theta) - r^P(t)\|_{L^2} + \lambda \cdot d_\angle \left(r^P(\infty;\theta), [\mathbf{b}]_{ron}/[\mathbf{d}]_{ron}\right)}_{J_1(\theta)+\lambda\cdot J_2(\theta)}, \\ \text{s.t.} \quad & \max_t x(t) < 0.8 \end{aligned} \tag{7}$$

where $[\mathbf{b}]_{ron}/[\mathbf{d}]_{ron}$ is the affinity vector of the odorant identity, and $\lambda \in \mathbb{R}_+$ is a scaling factor. The scaling factor λ controls the balancing between fitting DM4 physiology response vs. recovery of odorant affinity vector. The DM4 model response for different choices of λ is shown in **Fig.**11

4.5 Two-Step Optimization Procedure

Optimization of parameters for all models presented herein follow a two-step algorithm: 1) random sampling in the parameter space using Latin Hypercube Sampling [33], 2) fine tuning using Differential Evolution [34].

Step 1: Latin Hypercube Sampling (LHS) [33]

Latin Hypercube Sampling (LHS) is a method of generating random samples of parameter values from a multidimensional distribution. As opposed to random sampling (which generates samples uniformly along each dimension) or grid sampling (which generates samples at regular intervals along each dimension), LHS tries to optimize the random samples to satisfy the Latin Hypercube condition - one and only one sample is contained in each axis-aligned hyperplane. Specifically, a correlation-minimization optimization procedure was used to further randomize the initial uniform random samples in the work presented herein. The LHS routine utilized is adapted from scikit-optimize [35].

Step 2: Differential Evolution [34]

Differential Evolution (DE) is an evolutionary algorithm that seeks to solve a global optimization problem by iteratively improving candidate solutions. For the two-step optimization procedure, the initial candidate solutions are randomly sampled from a hypercube with each edge spanning the mean ± 1 standard deviation of parameter value along the top $N \sim 100$ parameter sets found using LHS sampling. During the DE optimization iterations, with a pre-specified *crossover probability*, randomly selected candidate solutions are recombined, and the recombinations in turn replaces the original candidate solutions if they result in a reduction in the optimization objective. The DE optimization procedure used in the current work is an accelerated version of the implementation in scipy [36].

References

[1] Quentin Gaudry, Katherine I Nagel, and Rachel I Wilson. Smelling on the fly: sensory cues and strategies for olfactory navigation in drosophila. Current opinion in neurobiology, 22(2):216–222, 2012.

[2] Aurel A. Lazar and Chung-Heng Yeh. A molecular odorant transduction model and the complexity of spatio-temporal encoding in the Drosophila antenna. PLOS Computational Biology, 16(4):e1007751, Apr 2020.

[3] Nicolas Y Masse, Glenn C Turner, and Gregory SXE Jefferis. Olfactory information processing in drosophila. Current Biology, 19(16):R700–R713, 2009.

[4] Yoshinori Aso, Daisuke Hattori, Yang Yu, Rebecca M. Johnston, Nirmala A. Iyer, Teri T.B. Ngo, Heather Dionne, L. F. Abbott, Richard Axel, Hiromu Tanimoto, and Gerald M. Rubin. The neuronal architecture of the mushroom body provides a logic for associative learning. eLife, 3:e04577, 2014.

[5] Andreas S Thum and Bertram Gerber. Connectomics and function of a memory network: the mushroom body of larval Drosophila, feb 2019.

[6] Rachel I Wilson. Early olfactory processing in drosophila: mechanisms and principles. Annual review of neuroscience, 36:217, 2013.

[7] Mark Stopfer, Vivek Jayaraman, and Gilles Laurent. Intensity versus identity coding in an olfactory system. Neuron, 39(6):991–1004, 2003.

[8] Kevin A. Bolding and Kevin M. Franks. Complementary codes for odor identity and intensity in olfactory cortex. eLife, 6:1–26, 2017.

[9] Charles F Stevens. What the fly's nose tells the fly's brain. Proceedings of the National Academy of Sciences, 112(30):9460–9465, 2015.

[10] Aurel A. Lazar and Chung-Heng Yeh. Predictive coding in the drosophila antennal lobe. In BMC Neuroscience 2019, 20 (Suppl 1): P353, Barcelona, Spain, July 2019. 28th Annual Computational Neuroscience Meeting.

[11] Aurel A. Lazar, Tingkai Liu, and Ching-Heng Yeh. An odorant encoding machine for sampling, reconstruction and robust representation of odorant identity. In IEEE International Conference on Acoustics, Speech and Signal Processing, pages 1743–1747, Barcelona, Spain, 2020.

[12] Hokto Kazama and Rachel I. Wilson. Homeostatic Matching and Nonlinear Amplification at Identified Central Synapses. Neuron, 59(1):183, jul 2008.

[13] PP Laissue, CH Reiter, PR Hiesinger, S Halter, KF Fischbach, and RF Stocker. Three-dimensional reconstruction of the antennal lobe in drosophila melanogaster. Journal of Comparative Neurology, 405(4):543–552, 1999.

[14] Qian Gao, Bingbing Yuan, and Andrew Chess. Convergent projections of drosophila olfactory neurons to specific glomeruli in the antennal lobe. Nature neuroscience, 3(8):780–785, 2000.

[15] Hokto Kazama and Rachel I Wilson. Origins of correlated activity in an olfactory circuit. Nature neuroscience, 12(9):1136–1144, 2009.

[16] Rachel I Wilson and Gilles Laurent. Role of gabaergic inhibition in shaping odor-evoked spatiotemporal patterns in the drosophila antennal lobe. The Journal of neuroscience, 25(40):9069–9079, 2005.

[17] Yuhua Shang, Adam Claridge-Chang, Lucas Sjulson, Marc Pypaert, and Gero Miesenböck. Excitatory local circuits and their implications for olfactory processing in the fly antennal lobe. Cell, 128(3):601–612, 2007.

[18] Shawn R Olsen and Rachel I Wilson. Lateral presynaptic inhibition mediates gain control in an olfactory circuit. Nature, 452(7190):956–960, 2008.

[19] Cory M Root, Kaoru Masuyama, David S Green, Lina E Enell, Dick R Nässel, Chi-Hon Lee, and Jing W Wang. A presynaptic gain control mechanism fine-tunes olfactory behavior. Neuron, 59(2):311–21, July 2008.

[20] Liang Liang and Liqun Luo. The olfactory circuit of the fruit fly drosophila melanogaster. Science China Life sciences, 53(4):472–484, 2010.

[21] Ju Huang, Wei Zhang, Wenhui Qiao, Aiqun Hu, and Zuoren Wang. Functional connectivity and selective odor responses of excitatory local interneurons in drosophila antennal lobe. Neuron, 67(6):1021–1033, 2010.

[22] Louis K Scheffer, C Shan Xu, Michal Januszewski, Zhiyuan Lu, Shin-ya Takemura, Kenneth J Hayworth, Gary B Huang, Kazunori Shinomiya, Jeremy Maitlin-Shepard, Stuart Berg, et al. A connectome and analysis of the adult *Drosophila* central brain. eLife, 9:e57443, sep 2020.

[23] Matthew E. Berck, Avinash Khandelwal, Lindsey Claus, Luis Hernandez-Nunez, Guangwei Si, Christopher J. Tabone, Feng Li, James W. Truman, Rick D. Fetter, Matthieu Louis, Aravinthan D.T. DT Samuel, and Albert Cardona. The wiring diagram of a glomerular olfactory system. eLife, 5(MAY2016):1–21, may 2016.

[24] Anmo J Kim, Aurel A Lazar, and Yevgeniy B Slutskiy. Projection neurons in drosophila antennal lobes signal the acceleration of odor concentrations. eLife, page e06651, 2015.

[25] Daniel Münch and C. Giovanni Galizia. DoOR 2.0 - Comprehensive Mapping of Drosophila melanogaster Odorant Responses. Scientific Reports, 6(October 2015):1–14, 2016.

[26] L. E. Givon and A. A. Lazar. Neurokernel: An open scalable software framework for emulation and validation of drosophila brain models on multiple gpus. Neurokernel Request for Comments, Neurokernel RFC #1, Feb 2014.

[27] Aurel A Lazar, Tingkai Liu, Mehmet Kerem Turkcan, and Yiyin Zhou. Accelerating with FlyBrainLab the discovery of the functional logic of the Drosophila brain in the connectomic and synaptomic era. eLife, 10, feb 2021.

[28] Thomas A. Cleland and Praveen Sethupathy. Non-topographical contrast enhancement in the olfactory bulb. BMC Neuroscience, 7, jan 2006.

[29] Shawn R Olsen, Vikas Bhandawat, and Rachel I Wilson. Divisive normalization in olfactory population codes. Neuron, 66(2):287–299, 2010.

[30] Masafumi Oizumi, Ryota Satoh, Hokto Kazama, and Masato Okada. Functional differences between global pre-and postsynaptic inhibition in the drosophila olfactory circuit. Frontiers in computational neuroscience, 6, 2012.

[31] Aaditya V Rangan. Functional roles for synaptic-depression within a model of the fly antennal lobe. PLoS Comput Biol, 8(8):e1002622, 2012.

[32] Stijn van Dongen and Anton J. Enright. Metric distances derived from cosine similarity and Pearson and Spearman correlations. arXiv, 2:2–6, aug 2012.

[33] M. D. McKay, R. J. Beckman, and W. J. Conover. A comparison of three methods for selecting values of input variables in the analysis of output from a computer code. Technometrics, 21(2):239–245, 1979.

[34] Rainer Storn and Kenneth Price. Differential Evolution – A Simple and Efficient Heuristic for global Optimization over Continuous Spaces. Journal of Global Optimization, 11(4):341–359, 1997.

[35] Tim Head, Manoj Kumar, Holger Nahrstaedt, Gilles Louppe, and Iaroslav Shcherbatyi. scikit-optimize/scikit-optimize. Oct 2021.

[36] Pauli Virtanen, Ralf Gommers, Travis E. Oliphant, Matt Haberland,

Tyler Reddy, David Cournapeau, Evgeni Burovski, Pearu Peterson, Warren Weckesser, Jonathan Bright, et al. SciPy 1.0: Fundamental Algorithms for Scientific Computing in Python. Nature Methods, 17:261–272, 2020.

5 Appendix

5.1 Temporal Processing of Mono-molecular Odorants Figure Supplements

Model Type	**Corresponding Components**	**D.o.F per Component**
Ionotropic Synapce	• OSN-to-PreLN synapse	3
Ionotropic Synapse with Fixed Rate Constants	• PostiLN-to-PN synapse • PosteLN-to-PN synapse • OSN Axon-Terminal-to-PN synapse	1
OSN Axon-Terminal	• OSN Axon-Terminal	4
OSN-to-PostLN Synapse	• OSN-to-PosteLN synapse • OSN-to-PostiLN synapse	8
Biophysical Spike Generator	• OSN Axon Hillock • PN Axon Hillock	0
Total		24

Table 2: Model and parameterizations for circuit shown in **Fig.**3(A[viii]), which is comprised of 9 components with a total of 24 parameters. Note that, rate constants for ionotropic synapses connected to the PN (i.e., OSN Axon-Terminal-to-PN, Post-iLN-to-PN and Post-eLN-to-PN) are fixed at $\alpha_1 = 100, \beta_1 = 100$, with the only free variable being the maximum conductance $\overline{g}_{max}$. Parameterization of other models shown in **Fig.**3(A) can be similarly calculated. For detailed model descriptions and formulations, refer to **Section** 4.3. *D.o.F* Degree of Freedom.

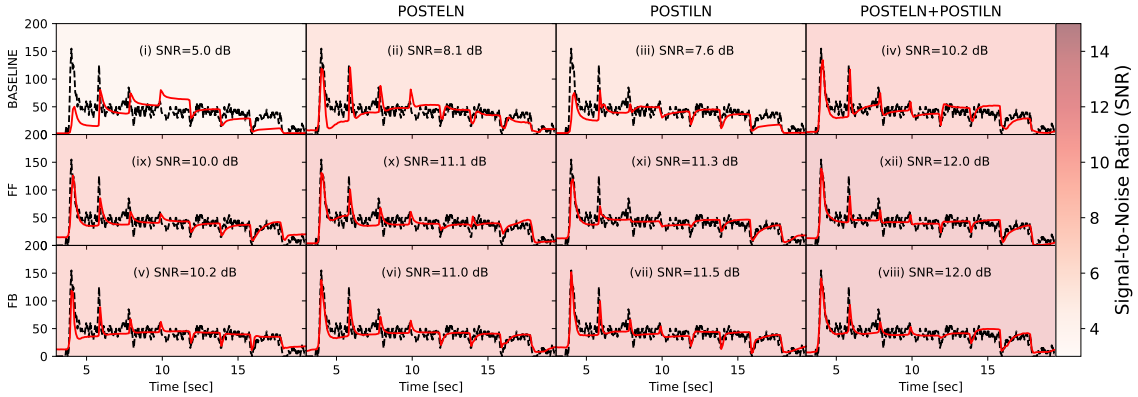

Figure 8: Best fitted temporal AL model responses to Acetone staircase waveform.

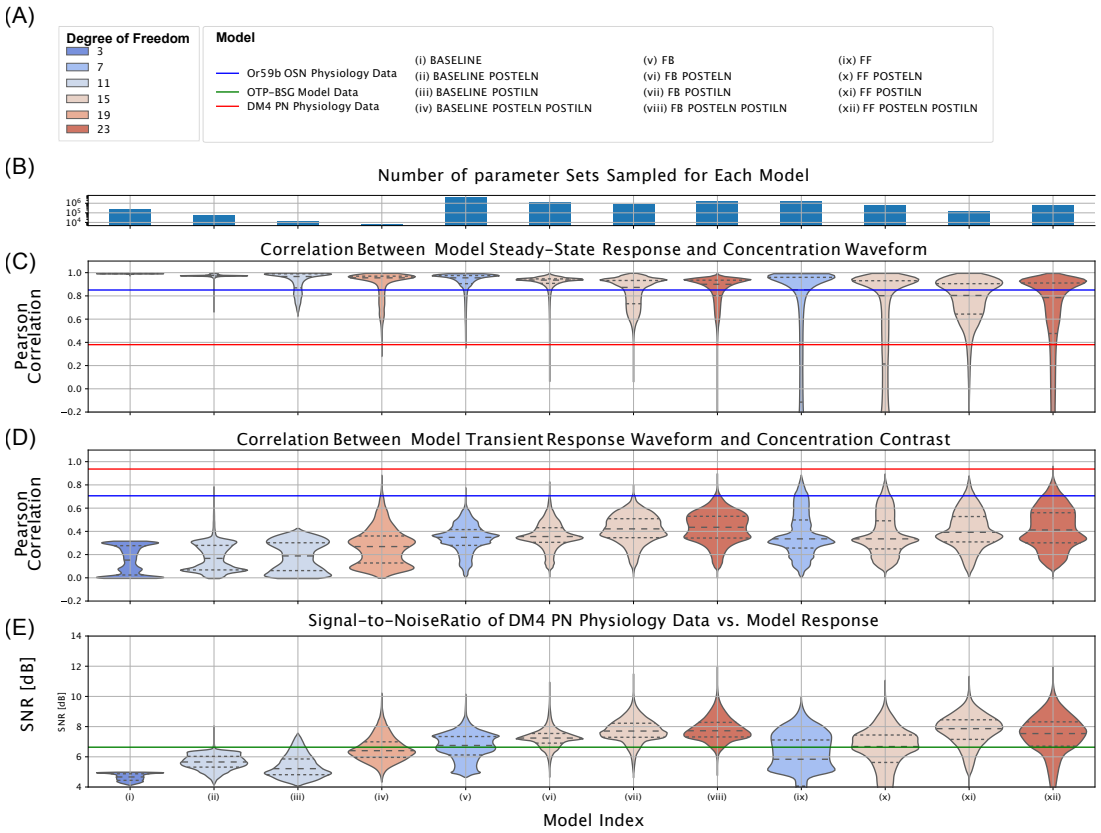

Figure 9: Comparison between models of Antennal Lobe for temporal processing of odorant input along single channel (Or59b OSN and DM4 glomerulus) for all 12 circuit architectures. (A) Legend for model and color reference for degree of freedom of each model. (B) Number of parameter sets sampled for each model. (C) Sample distribution of correlation between steady-state responses and concentration waveform over parameter space for each of the 8 models. The correlations between steady-state response and concentration waveform for DM4 PN and Or59b OSN physiology data are shown in red and blue for reference respectively. (D) Sample distribution of correlation between transient responses and concentration contrast over parameter space for each of the 8 models. The correlations between steady-state response and concentration waveform for DM4 PN and Or59b OSN physiology data are shown in red and blue for reference respectively. (E) Sample distribution of Signal-to-Noise Ratio between physiology recording data of DM4 PN and model responses. For refernece, the Or59b OSN physiology data is linearly scaled to achieve the best SNR against the DM4 PN physiology data. The SNR between the scaled OSN response and PN response is shown in blue.

5.2 Spatio-Temporal Processing of Mono-molecular Odorants Figure Supplements

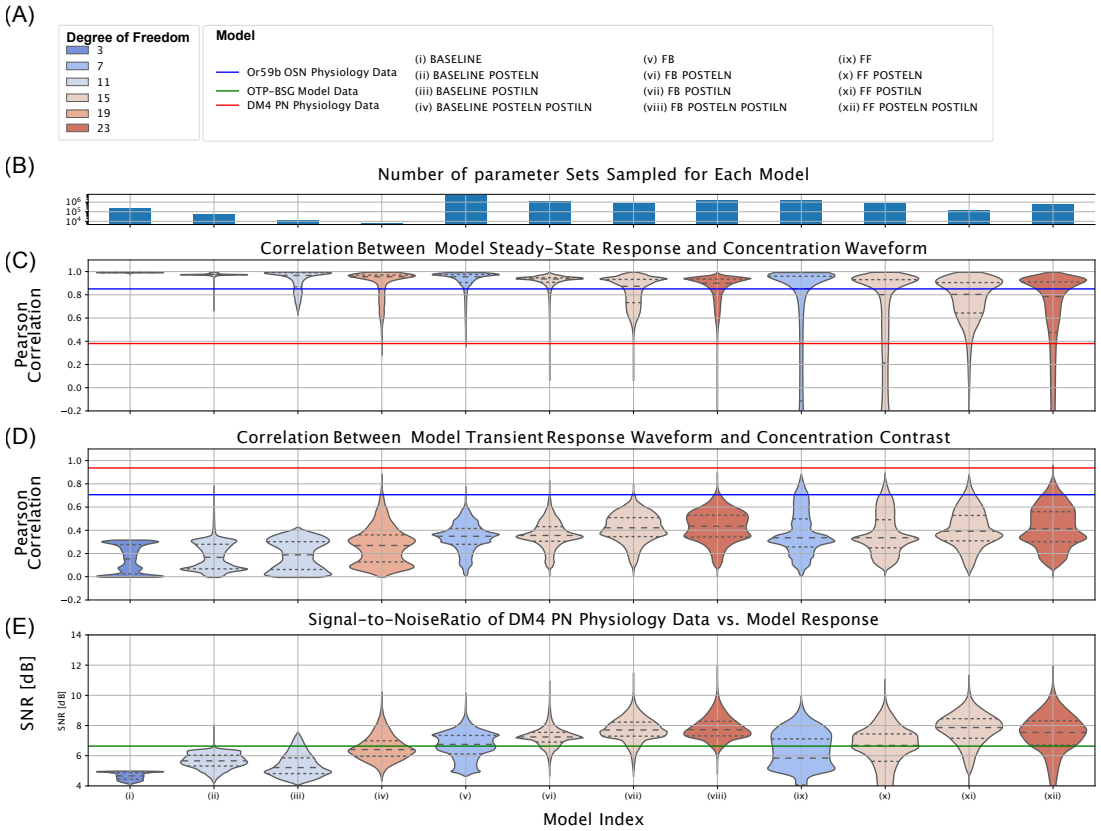

Figure 10: Global Feedforward/Feedback models of Antennal Lobe out perform Local Feedforward/Feedback models across parameterization. Comparison for all 20 circuit configurations. (A) Legend for model and degree of freedom. (B) Number of parameter sampled for each model. (C) Correlation between spatio-temporal model steady-state response in DM4 channel to staircase Acetone stimulus and concentration waveform. (D) Correlation between spatio-temporal model transient response in DM4 channel to staircase Acetone stimulus and concentration contrast. (E) Signal-to-Noise ratio between spatio-temporal model response in DM4 channel to staircase Acetone stimulus and physiology data. The distance between steady-state response of the OTP-BSG model and Acetone odorant affinity vector is shown in green for reference. (F) Average distance between spatio-temporal model responses and Acetone odorant affinity vector. The distance between steady-state response of the OTP-BSG model and Acetone odorant affinity vector is shown in green for reference.

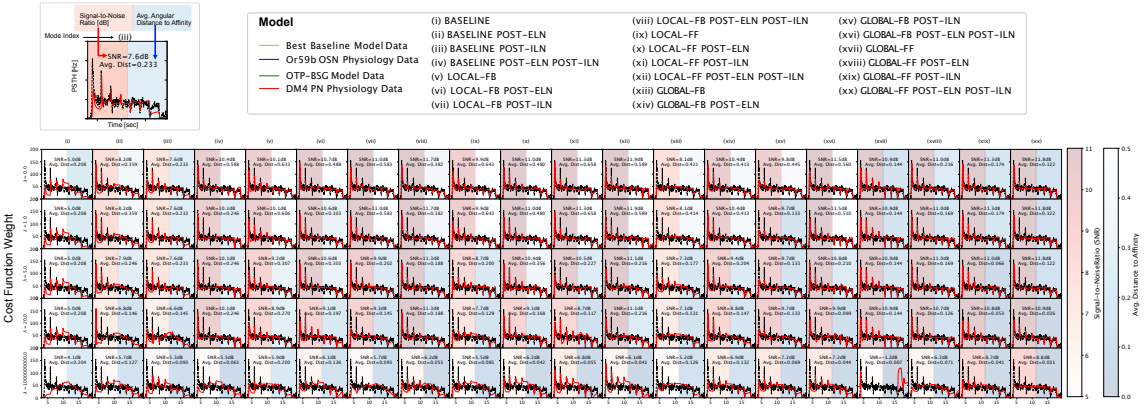

Figure 11: Spatio-Temporal model response to Acetone staircase waveform in the DM4 channel.